Multiscale SAXS-WAXD characterisation of the deformation mechanisms of electrospun PCL scaffolds

Multiscale SAXS/WAXD characterisation of the deformation mechanisms of electrospun PCL scaffolds

F. J. Camarena-Maese[1,2], F. Martínez-Hergueta[1,*], J. P. Fernández-Blázquez[3], R. W. Kok[1], J. Reid[4], A. Callanan[4]

[1] *School of Engineering, Institute for Infrastructure and Environment, The University of Edinburgh, William Rankine Building, EH9 3FG, Edinburgh, UK.*
[2] *Escuela Politécnica Superior. Universidad de Málaga. Avenida Cervantes, 2. 29071 Málaga. Spain.*
[3] *IMDEA Materials Institute. C/ Eric Kandel 2, 28906 Getafe, Madrid, Spain.*
[4] *School of Engineering, Institute for Bioengineering, The University of Edinburgh, Faraday Building, EH9 3JL, Edinburgh, UK.*

Abstract

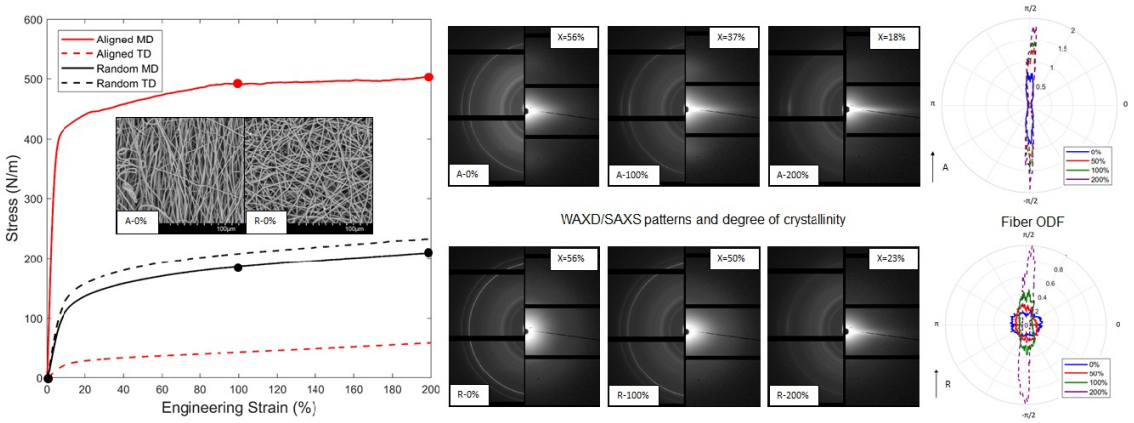

This research provides a thorough study of the mechanical response of PCL scaffolds and determines their deformation micromechanisms at different scales by a combination of experimental techniques (mechanical tests, scanning electron microscopy, wide angle X-ray diffraction and small-angle X-ray scattering). Scaffolds with different fibre orientation distribution functions were manufactured and subjected to tensile loading. Macromechanical properties were dictated by the fibre deformation and interaction in terms of fibre straightening, rotation and stretching. Stiffness and yield strength were directly proportional to the percentage of fibres oriented with the loading direction. Gradual deformation induced progressive fibre rotation, uncurling and stretching, showing different impact at molecular level for each configuration. Fibres aligned with the loading direction presented homogeneous

plasticity with an inherent loss of crystal phase, meanwhile misaligned fibres exhibited negligible loss of crystallinity due to a predominance of fibre rotation. Fibre plasticity triggered the macromechanical yielding of the scaffold and for high levels of plastic deformation fibres developed macromolecular fibrils and microvoids. These findings provide the fundamental observations to develop engineering tissues with highly tunable and tailored mechanical properties for site specific *in vivo* applications

Highlights

- In-situ SAXS/WAXD characterisation of PCL scaffolds is accomplished.
- Evolution of deformation mechanisms at different scales is ascertained.
- Contribution of fibre plastic deformation to the ductility of the scaffold is determined.
- Evolution of fibre orientation distribution function is presented.

Keywords: PCL scaffold, synchrotron, tensile response, SAXS/WAXD

1. Introduction

Polycaprolactone (PCL) scaffolds manufactured by electrospinning are a biocompatible artificial tissue that provide a feasible environment for cellular growth and nutrient delivery [1, 2, 3]. They achieve this by mimicking the microscale biophysical characteristics of the tissue being regenerated [4]. They have been successfully implanted in patients for reparation of resected osteosarcoma defects, dermis and cartilage [5, 6, 7], however, their weak mechanical properties hinder their implementation in applications that require higher stress solicitations such as bone or muscle [8, 9, 10].

Conventional characterisation of scaffolds usually focuses on biocompatibility and cell propagation [11, 12, 13], meanwhile, the study of their mechanical properties is currently marginal [14, 15, 16, 17, 18]. The mechanical properties of nonwovens can be analysed at a homogeneous network macroscale and at the individual fibre level. The global macroscale properties dictate cell bidding onto the scaffold, meanwhile, local microscale properties such

as resin stiffness and microthread volume play a secondary role in cell alignment [19, 20]. Analysis of mechanical properties and deformation mechanisms of PCL scaffolds under uniaxial stretching is usually accomplished by means of Scanning Electron Microscopy [21]. Mechanical response depends on both the stress state attained in the fibres and the way individual fibres interact with the network through the bonds. In particular, PCL scaffolds present outstanding ductility with variable stiffness proportional to fibre volume, bond density and the percentage of fibres oriented at a particular direction, known as fibre Orientation Distribution Function (ODF) [22, 23, 24]. When subjected to uniaxial stretch, the fibre ODF evolves in terms of fibre rotation and straightening, resulting in a modification of the original mechanical properties [25]. At the same time, fibres aligned with the loading direction are elastically, and eventually, plastically deformed [26]. Initial studies show certain similarities with the mechanical response of thermally bonded nonwovens [27, 28], however, a detailed study at molecular scale is required to fully understand the role of fibre plasticity and bond strength on the mechanical response of PCL scaffolds, which has a major role on the application and suitability of engineered tissues *in vivo* using this fabrication process.

Mechanical behaviour of PCL films at molecular scale is conventionally discerned by Wide-Angle X-ray Diffraction (WAXD) and Small-Angle X-ray Scattering (SAXS) [29]. WAXD is employed to detect the crystalline structure and orientation of the PCL phase, while SAXS is used to characterise the size and orientation of lamellae and amorphous regions. Diffraction techniques also show great potential to characterise the evolution of the deformation mechanisms of PCL scaffolds under uniaxial stretching and provide the relationship between fibre plasticity and macromechanical yielding. SAXS/WAXD analysis has been previously applied to determine the mechanical behaviour of fibre based materials such as Kevlar bundles [30], electrospun Poly(Vinyl Alcohol) nonwovens [31] and electrospun Nylon-6,6 fibres [32]. Diffraction techniques have been also employed to define the role of different processing parameters in the final microstructure of PCL scaffolds [33, 34, 35, 26, 36, 37], however, to the author's knowledge, inspection by simultaneous SAXS/WAXD of in-situ mechanical testing has not been accomplished before in this material.

The aim of this paper is to provide a thorough study of the mechanical response of PCL

scaffolds and determine their deformation micromechanisms at different scales, including for first time the molecular level. Scaffolds with aligned and random fibre ODFs were manufactured by electrospinning and characterised by a combination of experimental techniques. Scaffolds were initially inspected by scanning electron microscopy and subjected to tensile loading along perpendicular directions. Evolution of deformation mechanisms at network level in terms of fibre straightening, rotation and stretching was analysed for each configuration, focusing on the role of bond strength in the stress transfer mechanisms within the fibre network and the localisation of fibre plasticity as function of fibre orientation. Micromechanical characterisation at molecular level was carried out by means of SAXS/WAXD diffraction techniques, showing the relationship between crystal structure and fibre plasticity. SAXS intensity was also employed to quantify the evolution of fibre ODF. This information is relevant to determine the role of fibre plasticity in the macromechanical yielding of the scaffold. Furthermore, the reported mechanisms establishes the basis to predict and optimise the mechanical performance of engineering tissues and to develop highly tunable and tailored scaffolds for a wide range of applications with site specific *in vivo* requirements.

2. Materials and methods

2.1. Material

Scaffolds were manufactured by electrospinning with two different fibre distributions: aligned (A) and random (R). Fibres were produced by dissolving 10% polycaprolactone (PCL) in a solution of Hexafluoroisopropanol (97% purity, Manchester Organics, UK). Non-woven electrospun meshes were fabricated at flow rate of 1.2 ml h^{-1} through a needle bore of 0.4 mm, an accelerating voltage of +12 kV/ -4 kV and a working distance of 150 mm. All fibres were collected on a rotating mandrel covered with aluminium foil, at an ambient temperature of 23°C. Mandrel speed was set at 2000 rpm for aligned and 250 rpm for randomly distributed configurations. Further information about the manufacturing process is available in [38]. The manufacturing process introduced two principal material directions known as machine (MD) and transverse (TD) which followed the mandrel rotation and the

perpendicular direction, respectively. Morphology of the fibre network was inspected with a Hitachi TM400 Scanning Electron Microscope (SEM) with a 15 kV accelerating voltage and a working distance of 14 mm. Prior to SEM observation, stretched scaffolds were taped in a relaxed state onto an aluminium supporting plate.

2.2. Thermal characterisation

The fibre crystallinity was investigated by Differential Scanning Calorimetry (DSC) and Thermal Gravimetric Analysis (TGA). DSC was carried out in nitrogen atmosphere using a TA Instruments Q200 apparatus. Prior to testing, each specimen was weighted (5 mg) and placed in an aluminium pan, sealed with an aluminium cover. The specimen was heated at a rate of 20°C/min up to 120°C. The degree of crystallinity was calculated according to:

$$X = \frac{\Delta H}{\Delta H_0} \tag{1}$$

where ΔH_0 is the heat of fusion of 100% crystalline PCL, taken as 139.5 J/g [39] and ΔH is the heat of melting calculated by the integration of the melting peak for all samples [40].

TGA was carried out in nitrogen atmosphere (flow rate=200 ml min1) using a Seiko TG 220 at a heating rate of 10°C/ min in the temperature range from 20 to 800°C. Sample mass was 5 mg. TGA curves and derivatograms were recorded.

2.3. Mechanical testing

An Instron 3367 tensile test machine with a 50 N load cell was used to characterise the mechanical response of the scaffolds by means of stress-strain curves. Specimens were cut with scissors along perpendicular directions forming rectangles 60 mm long and 10 mm wide, with gauge length of 40 mm. Scaffolds were stretched up to a 200% of deformation at a constant velocity of 0.25 mm/s. Conventional force per width values were used to normalise the material stress, as established by the standard test method for 2D materials (ASTM D5729-97). Scaffolds were characterised along the machine (MD) and transverse (TD) directions and three samples were tested per configuration to determine the scattering in mechanical properties.

2.4. Microstructural SAXS/WAXD characterisation

Simultaneous Wide-Angle X-ray Diffraction (WAXD) and Small-Angle X-ray Scattering (SAXS) data were collected at the I22 beamline of the Diamond Light Source synchrotron facility (Didcot, Oxfordshire, UK) [41]. The beamline was tuned to operate at a beam energy of 12.4 keV giving a wavelength of 1 $\mathring{A}$. WAXD and SAXS measurements were performed over a 250 x 80 μm^2 spot size, with sample-to-detector distances of 400 and 4780 mm, respectively. The two-dimensional X-ray patterns were recorded on Pilatus P3-2M detectors with a 1 s exposure time. Scaffolds with random and aligned architecture were analysed to different degrees of elongation along MD and TD directions. Measurements were taken in-situ, while the scaffolds were stretched in a small elongating frame actuated at a constant velocity of 2 mm/s .

2.5. Data analysis

Raw synchrotron data were directly processed with the software DAWN [42, 43]. Pipelines linking the calibration and mask files were programmed and background intensities were extracted from the patterns to remove the influence of the exposure time and the Kapton window. Azimuthal and radial integrations were computed and results were exported in csv files for further data treatment with the software MATLAB [44].

The scanning records for WAXD were focused on the q-spacing 1.4 $\mathring{A}^{-1} < d < 1.8\ \mathring{A}^{-1}$ which covered the diffraction peaks corresponding to (110), (111) and (200) planes of the orthorhombic lattice structure of PCL crystals [45]. Radial integration of 2D WAXD patterns within the interval 105° to 355° was accomplished to obtain the one-dimensional graph in the form of normalised intensity (area under the curve equals to 1) *vs* q in Angstrom. As samples of the pure amorphous material could not be manufactured, the degree of crystallinity was obtained by deconvoluting the crystalline phase of the main diffraction peaks (110) and (111) with a Gaussian fit. Degree of crystallinity was calculated according to equation:

$$X = \frac{I_c}{I} \tag{2}$$

where I_c stands for the total crystalline area under the Gaussian curves and I represents the total area given by the diffractogram in the range 1.4 to 1.6 $\mathring{A}^{-1}$.

Data treatment of SAXS patterns was divided into low and high q-spacing values. Long period (L, distance between the adjacent lamellae) was obtained from the outer q range 0.03 to 0.08 $\mathring{A}^{-1}$ and was calculated from the Bragg equation:

$$L = \frac{2\pi}{q_{max}} \tag{3}$$

where q_{max} corresponded to the scattering maximum position from the Lorentz-corrected 1D SAXS curves [40, 46]. Integration of 2D SAXS patterns was accomplished in equatorial and meridional regions separately to isolate the signal provided by the long period with equivalent cake amplitudes of 80°, centered on the equator (π) and the pole ($\pi/2$) respectively.

Low q-spacing region was postprocessed to obtain the fibre Orientation Distribution Functions (ODFs) following an equivalent methodology based on the analysis of WAXD patterns previously validated for different fibre networks [47, 48, 49]. Advantage of this technique with respect to conventional Fourier transform image processing of micrographies obtained by scanning electron microscopy or confocal laser scanning microscopy is the versatility for thick materials [50]. Methodology to obtain the equivalent fibre ODF is recalled in this section for the shake of completion.

The distribution of azimuthal intensity of the diffraction pattern is directly proportional to the alignment of the polymer chains for WAXD, and macromolecular arrangements for SAXS. Statistically, the diffraction patterns provide the distribution of average tangent orientation vectors within the inspection spot, hence patterns will present a constant intensity if the vectors are isotropically oriented in all directions or will show discrete spots parallel to the vector direction in the case of perfect alignment along the preferential direction. The level of preferred lamellar and macromolecular orientation in a fibre depends on the material, the manufacturing process and the stretching of the fibre [33]. In the particular case of electrospun PCL fibres, a low degree of misorientation is expected for large macromolecular arrangements such as fibrils and cavitations [30, 51, 52, 53, 54, 26], therefore, the inner region of the SAXS signal at low q values can limit the error in the resultant fibre ODFs when assuming perfect alignment of the average tangent vectors with the fibre axis.

The scanning records were centered in the range 0.02 to 0.025 $\mathring{A}^{-1}$. Considering a curved

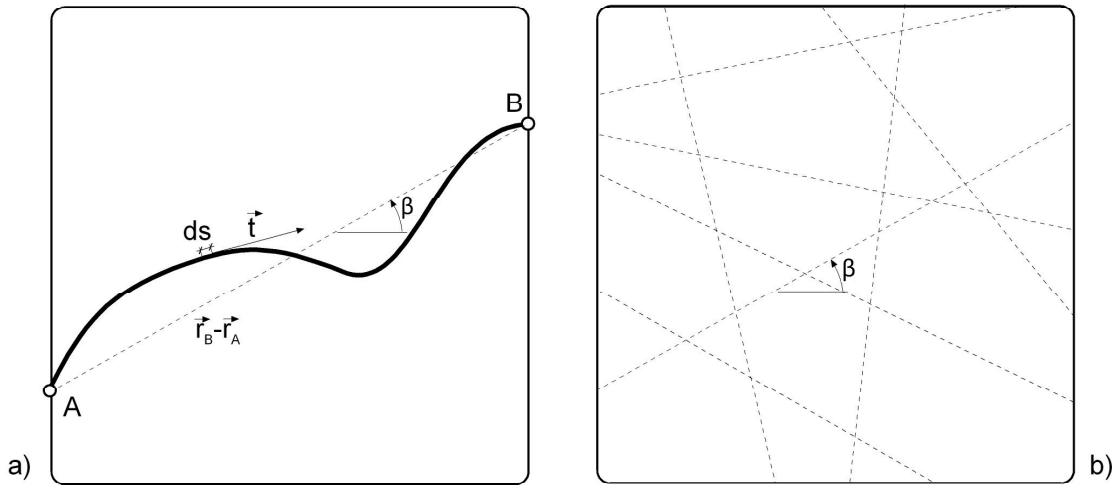

Figure 1: (a) Planar representation of a curved fibre within the inspection spot of the SAXS measurement. The end-to-end orientation vector, $\langle \vec{t} \rangle$, can be used to track the fibre orientation. (b) Distribution of end-to-end vectors in the electrospun scaffold.

fibre, as the one depicted in Fig. 1, the average tangent direction, $\langle \vec{t} \rangle$, can be determined as

$$\langle \vec{t} \rangle = \frac{1}{L} \int_A^B \vec{t}\, ds = \frac{\vec{r}_B - \vec{r}_A}{L} \tag{4}$$

which can be understood as a measure of the orientation angle, β in Fig. 1(a), of a fictitious straight fibre joining the fibre ends (end-to-end vector, A to B points), see Fig. 1(b). The angular distribution of average orientation vectors within the inspection spot can be considered representative of the overall fibre ODF in the scaffold. Intensity values were normalized to obtain an area equal to 1 under the ODF function for comparison purposes. This treatment encompasses both fibre curvature and fibre orientation and it is not possible to deconvolve them. It should be noted that, although the spot size was much smaller than the fibre length, this methodology has been previously validated through 3D X-ray microtomography for UHMWPE nonwovens, were fibre ODFs obtained by both techniques were in good agreement [49]. The beam spot size was also of same order of magnitude of SEM micrographies, so conventional hypothesis regarding fibre length and fibre orientation considered for fast Fourier transform image analysis of SEM micrographies should still be valid [22, 33, 50, 24].

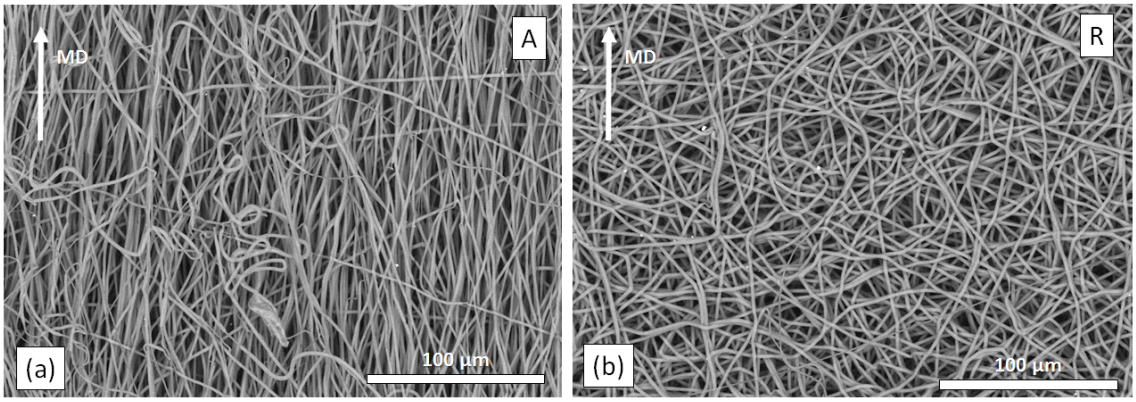

Figure 2: Different architectures of the manufactured scaffolds. (a) Aligned and (b) random configurations.

3. Results and discussion

3.1. Morphological characterisation

Manufactured scaffolds were initially inspected by SEM. Scaffolds were processed with different fibre distributions: aligned (A) and random (R), see Fig.2 (a) and (b), respectively. All fibres were composed of a single filament and two different fibre diameters of 1.435 ± 0.277 μm and 1.894 ± 0.166 μm were obtained for the aligned and random configurations respectively. The random scaffold exhibited high fibre curvature, meanwhile the aligned scaffold was mainly composed of straight fibres, although a percentage of fibres with high curvature appeared as a result of fibre breakage during electrospinning. Fibre bonds were created by local fusion when fibres deposited in the collector had not dried completely such that adjacent fibres fused together when the solvent evaporated.

3.2. Thermal characterisation

Thermal behaviour of the scaffolds was also analysed by TGA and DSC, see Fig. 3. Similar results were found for both, aligned and random configurations. The thermogravimetric analysis showed negligible mass loss until approximately 400°C, where full decomposition of the PCL scaffolds was registered. No evidence of any additional component apart from the PCL polymer was found. The differential scanning calorimetry detected the melting peaks around 61°C, with enthalpies of 79.4 and 75.8 J/g for aligned and random configurations

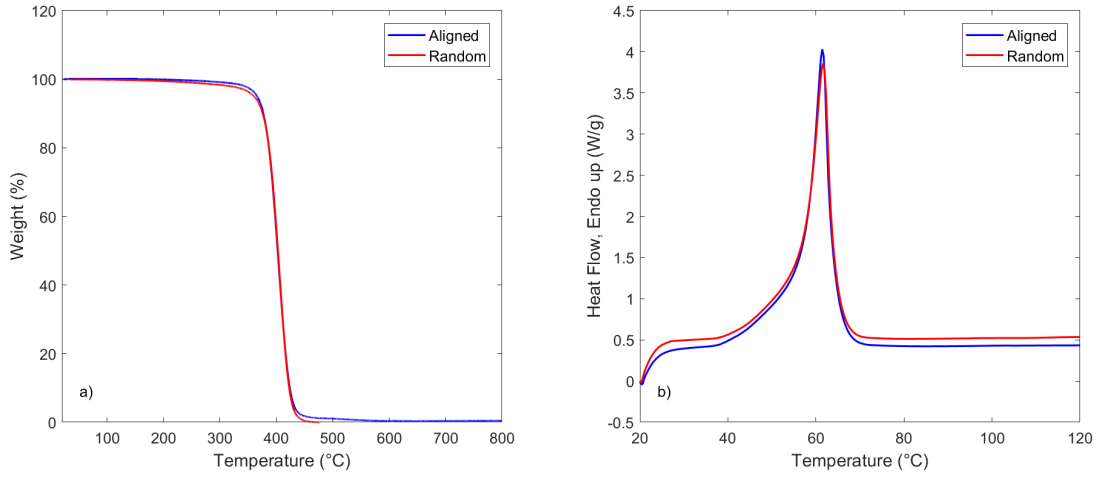

Figure 3: Thermal characterisation of aligned and random PCL scaffolds. (a) Thermogravimetric analysis (TGA) and (b) differential scanning calorimetry thermograms (DSC).

respectively and equivalent crystallinities of 57% for aligned and 54.3% for random scaffolds with an average of 55.7%, in agreement with previous observations [39, 55].

3.3. Macromechanical response

The tensile response of the scaffolds was characterised along machine (MD) and transverse (TD) directions. Representative nominal stress (force per fabric width) *vs.* engineering strain curves are plotted in Fig. 4. The average values of the yield stress, yield strain, the Young's modulus and plastic area slope are depicted in Table 1, together with the standard deviation, as a function of the loading direction. Higher scattering in material properties was given for the aligned scaffold stretched along MD due to slippage from the grips. All configurations showed an initial elastic response followed by a plastic region, exhibiting outstanding ductility up to 200% strain without attaining final failure. Yielding occurred when the fraction of fibres oriented with the loading direction plasticised.

Differences in mechanical properties for each tested configuration were dictated by micromechanical deformation mechanisms such as fibre straightening, rotation and stretching, therefore, macromechanical parameters such as scaffold stiffness, strength and yield strain depended on the initial fibre Orientation Distribution Function (ODF). As shown in Fig. 4,

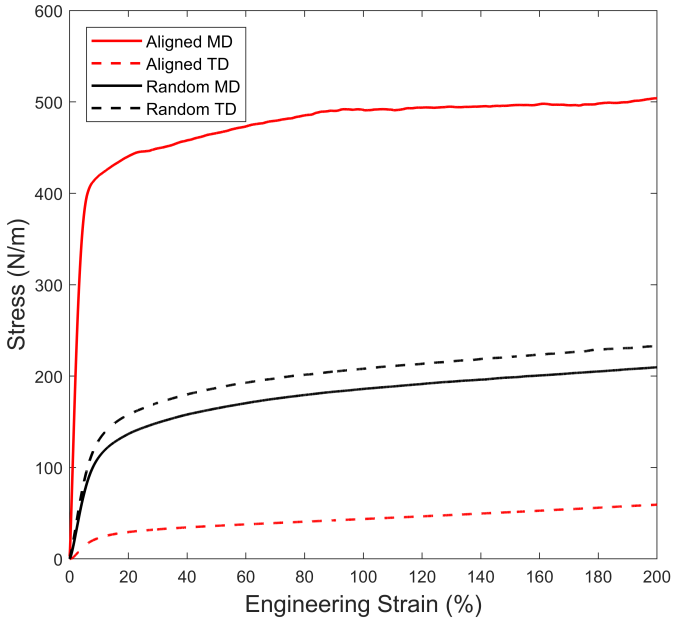

Figure 4: Representative nominal stress *vs.* engineering strain curves for the aligned and random scaffolds along machine and transverse directions.

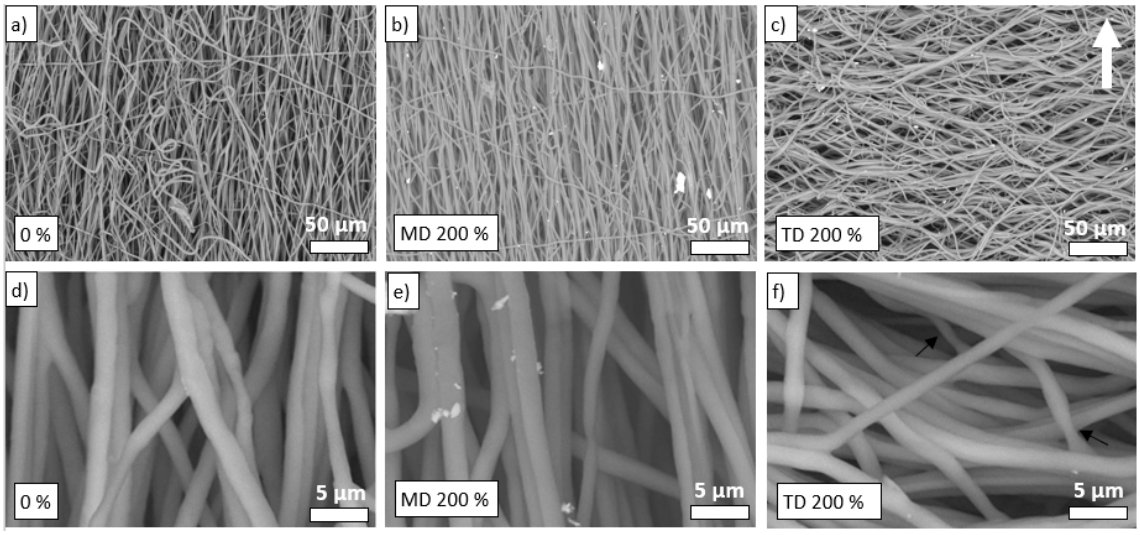

Figure 5: Above, SEM images of aligned scaffolds (a) 0%, (b) 200% along MD and (c) 200% along TD strain. Below, respective higher magnifications. The white arrow indicates the direction of stretching and the black arrows show local fibre necking.

Table 1: In-plane tensile mechanical properties of the aligned and random scaffolds as a function of the orientation

Type	Loading direction	Yield stress (N/m)	Yield strain (%)	Young's modulus (N/m)	Plastic area slope (N/m)
Aligned	MD	438.7±6.1	6.75±1.02	6499.3±130.18	98.76 ±26.25
	TD	25.9±2.8	13.2±1.22	191.6±3.3	14.88 ± 0.13
Random	MD	116.2±11.8	11.05±0.88	1051.4±24.0	25.23 ±1.98
	TD	130.3±11.5	11.66±0.87	1145.7±20.7	27.20 ± 1.15

the aligned scaffold presented very different mechanical response when tested along the machine (MD) and the transverse (TD) directions, exhibiting 30 times higher stiffness and 17 times higher yield strength when stretched along MD than along TD. These differences on stiffness and yield strength were a result of the greater percentage of fibres oriented with the loading direction, as shown in Fig. 5(a). The fibre ODF also had a significant influence on the triggering of the macromechanical plasticity of the scaffold, exhibiting higher yield strain for TD configuration rather than along MD.

Mechanical properties of the aligned scaffold across perpendicular directions were dictated by the triggering sequence of deformation micromechanisms. Fibre deformation became the predominant deformation mechanisms when stretching along the stiffest direction (MD) with negligible influence of fibre rotation, as depicted by the evolution of fibre morphology for a 200% of deformation in Fig. 5(b). As a result of the low fibre curvature, fibre plastification of aligned fibres was homogeneous, as shown in the micrography at higher magnification, see Fig. 5(e). On the other hand, when stretching along transverse direction (TD), the scaffold presented the softest response, with higher yielding strain and lower moduli. The predominant deformation mechanism was fibre rotation, as shown by the evolution of the fibre ODF at 200% of deformation in Fig. 5(c). Large fibre rotation took place before fibre plastification became significant to trigger macromechanical yielding, presenting local necking of a small fraction of fibres, see Fig. 5(f). The fibre rotation delayed the macrome-

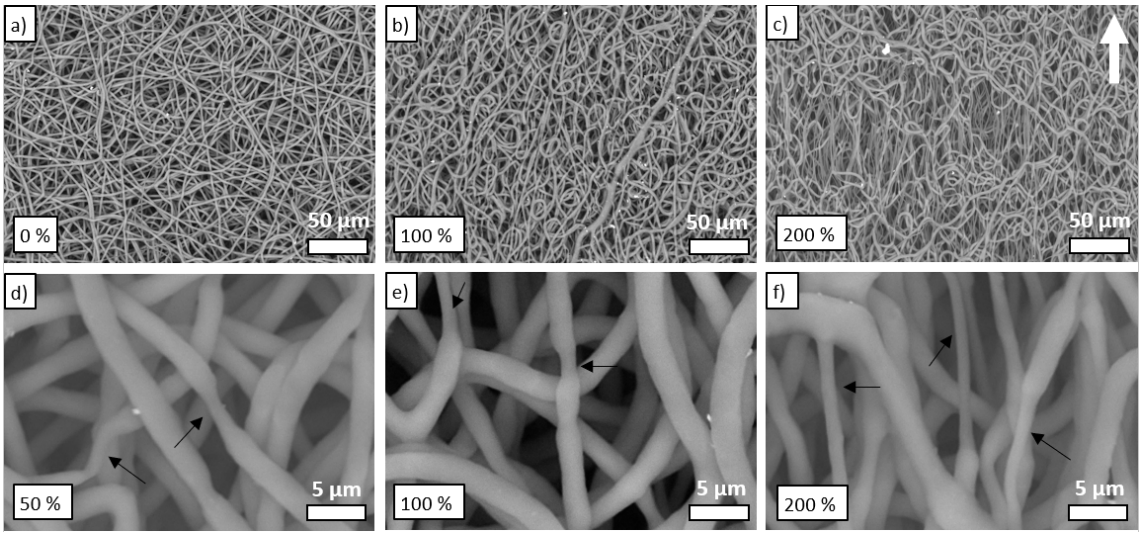

Figure 6: Above, SEM images of random scaffolds (a) 0%, (b) 100% and (c) 200% strain. Below, higher magnifications for (d) 50%, (e) 100% and (f) 200% strain. The white arrow indicates the direction of stretching and the black arrows show local fibre necking.

.

chanical yielding of the scaffold, increasing the yield strain from 6.75% (MD stretching) up to 13.2% of deformation, see Table 1. After the yielding strain, bonds between fibres ensured the stress transfer leading to further progressive realignment with the loading direction. The combination of fibre rotation and localised plastification resulted in a plastic slope and equivalent hardening modulus six times lower when stretching along TD, compared to the MD direction, driven solely by fibre global plastification. Bonds also controlled the evolution of the fibre ODF anchoring fibres at discrete points of the network, resulting in an increment of fibre curvature instead of bond fracture and fibre sliding [56].

The random scaffold exhibited an intermediate behaviour due to the coupling of fibre uncurling, rotation and stretching. All values of stiffness and strength were within the bounds given by the mechanical properties of the aligned scaffold across perpendicular directions, although higher proximity to the mechanical response of the aligned scaffold tested along transverse direction (TD) was found. Slightly higher stiffness and strength were exhibited when stretching along TD, however, overall response of the material was considered homogeneous, with quasi-isotropic fibre ODF, bond density and fibre connectivity, see Fig. 6(a). As

elongation progressed, fibre uncurling and re-orientation occurred heterogeneously, showing regions of high fibre re-alignment and regions that preserved the original fibre curvature, see Figs. 6(b) and (c). Fibres oriented with the loading direction exhibited heterogeneous global plasticity and localised necking, see Figs. 6(d) and (e), which became the predominant deformation mechanisms at high strain levels, see Fig. 6(f). This phenomenon of local necking ocurred due to the high adhesion of the bonds between fibres. As opposed to thermally bonded nonwovens [28], the bonds originated during electrospinning presented high resistance and did not fail at large strains. As a result, anchoring points possessed the largest structural section, inducing necking of adjacent single filaments.

3.4. WAXD and SAXS analysis

WAXD and SAXS measurements where taken in-situ simultaneously during deformation to analyse the microstructural evolution for different strain levels. Figs. 7 and 8 show the representative WAXD and SAXS patterns for aligned scaffolds stretched along MD and TD respectively, and Fig. 9 shows the equivalent for the random configuration. For the as-received state, the corresponding two main reflections (110) (innermost) and (200) (outermost) were identified on the 2D WAXD patterns. Preferential fibre alignment was qualitatively exhibited in the (200) diffraction peak, which appeared as an azimuthal arc oriented parallel to the fibre axis, on the equatorial region for the MD aligned scaffold, see Fig. 7(a), and on the equivalent meridional region for the TD scaffold, see Fig. 8(a), meanwhile, the random scaffold presented an homogeneous circular ring as a result of the isotropic fibre arrangement, see Fig. 9(a). The patterns evolved with deformation, re-orienting with the loading direction, changing the angular position and width of the diffraction peaks and showing different evolution trends for each configuration.

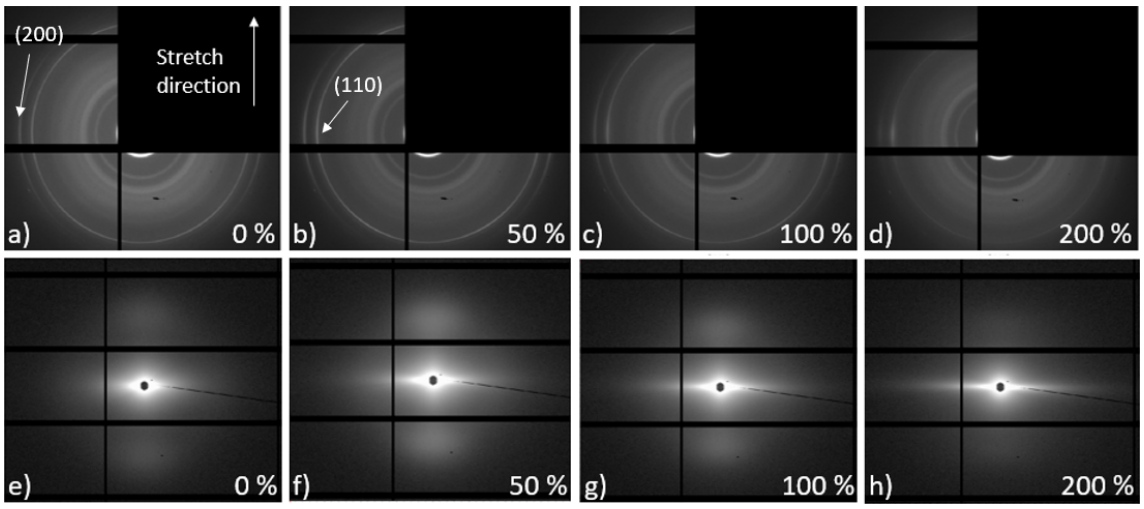

Figure 7: Above, two-dimensional WAXD patterns of aligned scaffolds stretched along MD. (a) 0%, (b) 50%, (c) 100% and (d) 200%. Below, two-dimensional SAXS patterns of scaffolds with the same configuration. (e) 0%, (f) 50%, (g) 100% and (h) 200%.

.

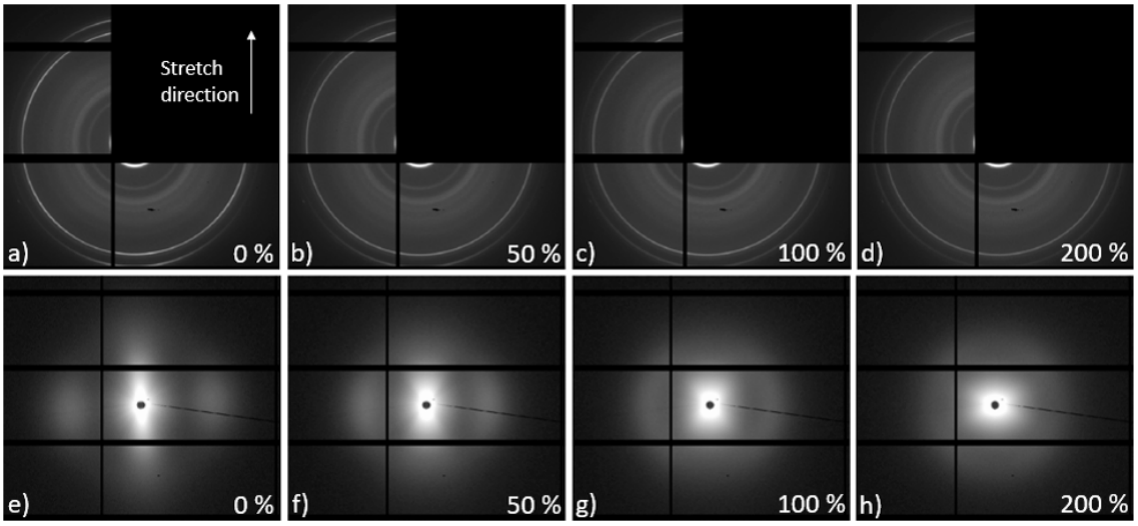

Figure 8: Above, two-dimensional WAXD patterns of aligned scaffolds stretched along TD. (a) 0%, (b) 50%, (c) 100% and (d) 200%. Below, two-dimensional SAXS patterns of scaffolds with the same configuration. (e) 0%, (f) 50%, (g) 100% and (h) 200%.

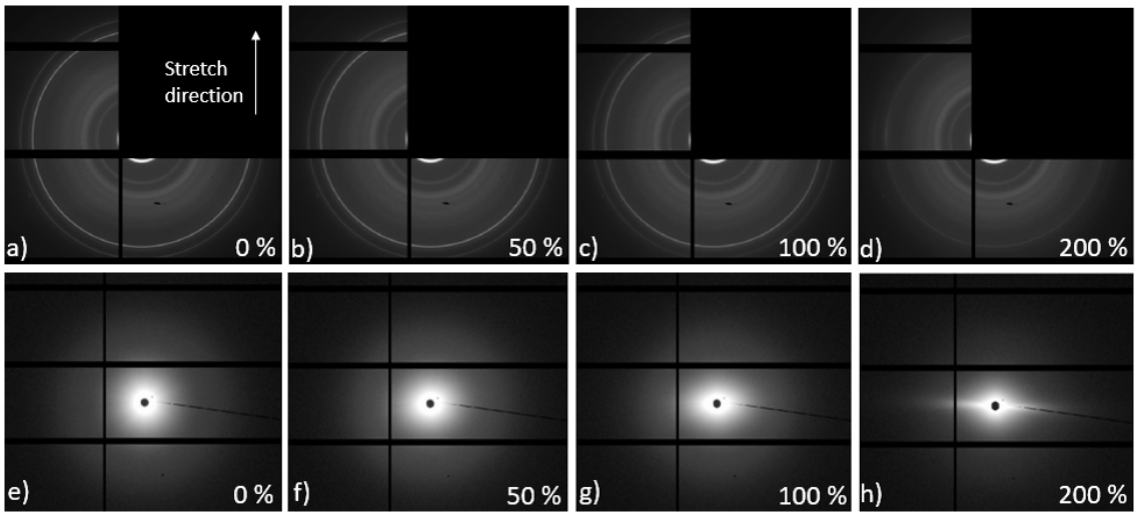

Figure 9: Above, two-dimensional WAXD patterns of random scaffolds. (a) 0%, (b) 50%, (c) 100% and (d) 200%. Below, two-dimensional SAXS patterns of scaffolds with the same configuration. (e) 0%, (f) 50%, (g) 100% and (h) 200%.

To offer quantitative information of the evolution of the crystalline structure, 1D-WAXD curves integrated over the planar area from the corresponding 2D-WAXD patterns are plotted in Fig. 10 for different deformation levels. As elongation progressed, peaks broaden indicating a change in the crystal morphology. Degree of crystallinity was determined using the methodology exposed in previous Section 2.5 and results are plotted in Fig. 11. All configurations presented a similar initial crystallinity degree, between 55 to 60%, in agreement with the DSC measurements, exhibiting a different trend with elongation depending on the predominant deformation mode. As mentioned before, main deformation mechanism of the aligned scaffold stretched along TD was fibre rotation with the loading direction with minimal localised plasticity at fibre necks, therefore, deformation process had negligible impact at crystal (lamella) level, showing reduced evolution of crystallinity. On the other hand, main deformation mechanism of aligned scaffolds elongated along MD was fibre stretching, exhibiting continuous reduction of fibre crystallinity up to a 18% for 200% of deformation. At the same time, the mechanical response of the random scaffold coupled stretching, rotation and straightening of the fibres, showing drastic decrease of crystallinity after a 100% of deformation corresponding to homogeneous plastification of a large fraction of fibres aligned

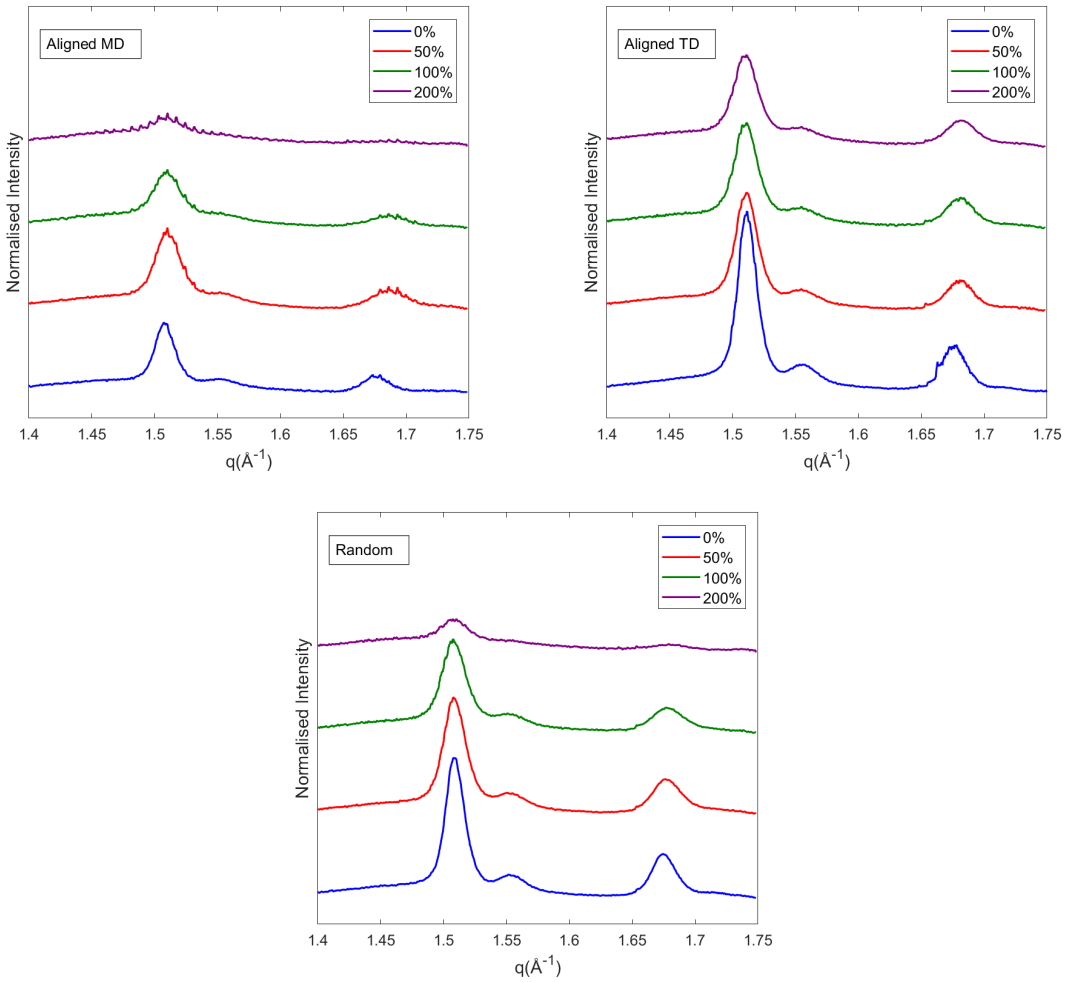

Figure 10: Evolution of 1D-WAXD curves with deformation for (a) aligned scaffold stretched along MD, (b) aligned scaffold stretched along TD and (c) random scaffold.

with the loading direction, in agreement with previous SEM observations, see Fig. 6(c). As reported in previous studies [57], loss of crystal phase was a result of lamellae fragmentation. Fibre deformation over the yield strain unfolded the crystalline molecular chains increasing the content of amorphous phase. As a result of this phenomenon at molecular scale, scaffolds suffered macromechanical yielding, see Fig.4.

Further evolution of the crystal structure was analysed by SAXS. Two different regions were identified; the outer region at high q values, representative of the distance between lamellae and the inner region at low q values, produced by macromolecular arrangements

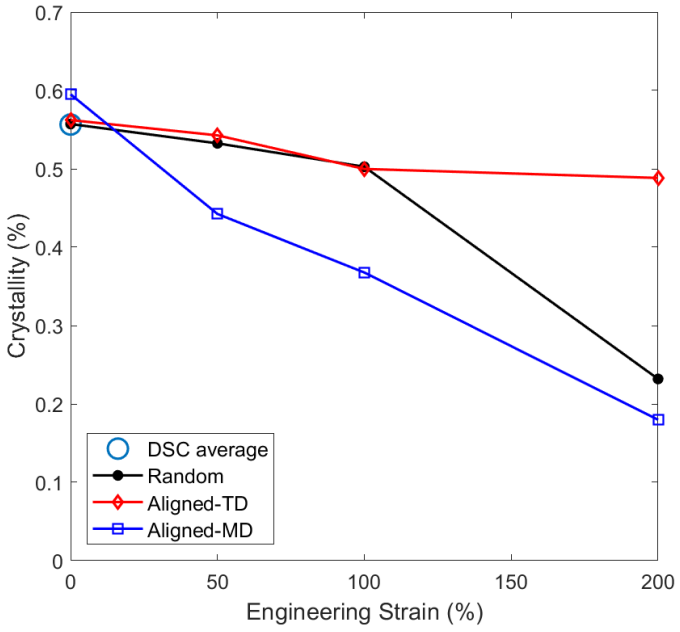

Figure 11: Evolution of the degree of crystallinity with deformation and validation with DSC results.

[30]. The preferential fibre alignment can be also observed in the outer scattering patterns, with a dumbbell-like signal perpendicular to the fibre axis; at the meridional region for MD aligned scaffold, see Fig. 7(e), and at the equatorial region for the TD aligned scaffold, see Fig. 8(e), in line with WAXD observations. Again, the random scaffold presented an homogeneous scattering ring, see Fig. 9(e). Evolution of scattering signals with deformation followed the macrostructural fibre rotation and the changes at fibre molecular level. The homogeneous ring of the random scaffold transformed from circular to oblate progressively due to the reorientation of the fibres with the loading direction, see Figs. 9(f), (g) and (h). On the other hand, the TD aligned scaffold turned from oblate to circular due to the increment in fibre curvature, see Figs. 8(f), (g) and (h). Finally, the MD aligned scaffold kept the original dumbbell-like shape as fibre re-alignment was limited, see Figs. 7(f) and (h).

The outer region cake integrations of 2D SAXS patterns at high q values are shown in Fig. 12. Two characteristic long periods were identified; $L_0 = 126.6\mathring{A}$ for the as-received state, and $L = 148.4\mathring{A}$ for stretched specimens. The random scaffold additionally presented

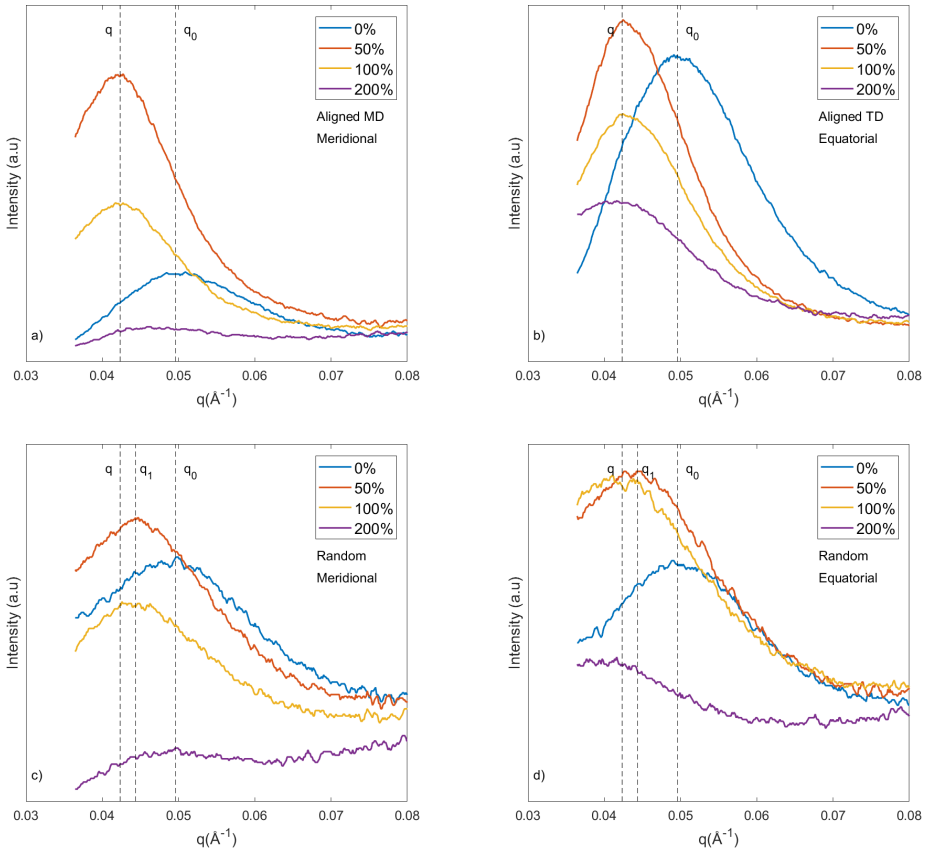

Figure 12: Evolution of 1D-SAXS curves with deformation for (a) Aligned scaffold stretched along MD, meridional integration, (b) aligned scaffold stretched along TD, equatorial integration, (c) random scaffold, meridional integration and (d) random scaffold, equatorial integration. Dashed lines mark the scattering maximum for as-received state ($q_0 = 0.0496\mathring{A}^{-1}$), partial elastic deformation ($q_1 = 0.0444\mathring{A}^{-1}$) and saturation of elastic deformation ($q = 0.0432\mathring{A}^{-1}$).

an intermediate value $L_1 = 141.7\mathring{A}$ for a 50% of deformation. The long period measured the distance between adjacent lamellae consisting of amorphous and crystalline regions and its shift towards a lower scattering angle indicated an increment of deformation of the amorphous regions. This microstructural change translated into recoverable elastic deformation of the fibres and it was triggered before lamellae fragmentation. Macromechanically, aligned scaffolds composed of straight fibres exhausted the elastic deformation capacity at a 50% of elongation, meanwhile, the random scaffolds still presented remaining elasticity as a result of the high fibre curvature previously registered by SEM microscopy, see Fig. 6.

Additionally, evolution of signal intensity was also registered for all configurations. An increment of intensity was exhibited from 0 to 50% of deformation mainly produced by the homogenisation of the distances between amorphous and crystalline regions, with an inherent reduction of the peak width. On the other hand, deformations higher than 50% induced a reduction of the signal intensity due to the fibre rotation, that spread the scattering signal out of the selected integration range, and the loss of crystal phase, in agreement with previous crystalinity measurements, see Fig. 11. Equatorial measurements were also influenced by the generation of a streak, represented by an increment of signal for low scattering angles, not related to the long period. These observations differed from previous results in PCL films, where strain-induced recrystallisation occurred in the amorphous region, developing a newly formed polymorph of smaller crystals characterised by a lower long period [29]. The current results suggest that the manufacturing of fibres by electrospinning inhibits the strain-induced recrystallisation process due to the high degree of molecular orientation. Please note Fig. 12 represents three different in-situ experiments, so comparisons of the non-normalised intensity signal between different samples should be carefully assessed. Intensity counts are heavily influenced by macromechanical parameters such as electron density, scaffold density, air voids, relative position of the sample in the holder, beam focus, etc. Differences were also potentiated by the non-symmetric nature of the beam spot produced by two different adaptive bimorph vertical and horizontal mirrors [58].

At an upper scale, further observations can be extracted from the inner region of SAXS patterns at low q values. Azimuthal integrations of the SAXS signals as described in previous Section 2.5 were computed to obtain the evolution of the fibre ODFs, see Fig. 13 (a) and (b) for aligned scaffold stretched along MD and TD respectively, and (c) for the random scaffold. The aligned scaffolds initially had around 90% of fibres oriented with the MD, meanwhile, the random scaffold presented a nearly homogeneous fibre distribution with slightly higher percentage of fibres oriented with the TD. These observations were in agreement with the mechanical response of the random scaffold, that exhibited slightly higher stiffness along TD, see Fig. 4. The deformation of the scaffold promoted a progressive fibre re-orientation with the applied strain along the $\pi/2$ and $-\pi/2$ loading directions, showing different trends

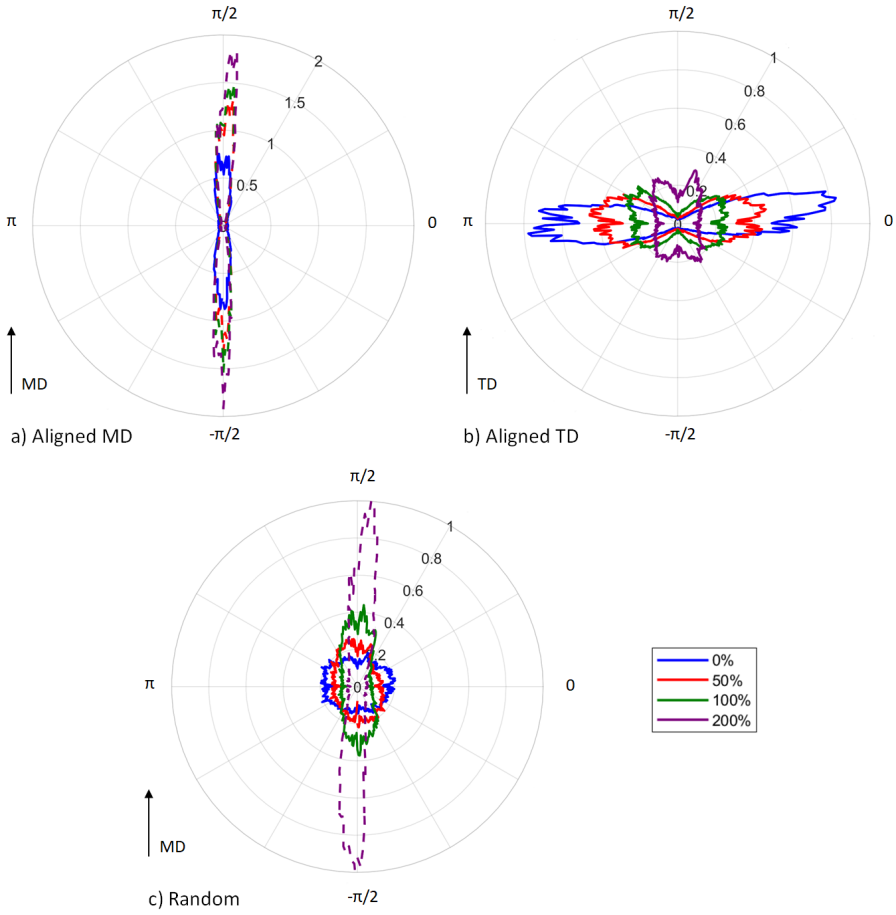

Figure 13: Polar representation of the evolution of the fibre orientation distribution function (ODF) as function of the applied strain. (a) Aligned scaffold stretched along MD, (b) aligned scaffold stretched along TD and (c) random scaffold. Dash lines stand for the summation of the fibre ODF and the newly developed macromolecular arrangements.

depending on the initial fibre ODF. In particular, the aligned scaffold stretched along TD gradually lost the initial unidirectional structure, resulting in a bimodal fibre distribution as a result of the induced fibre curvature. On the other hand, the random scaffold progressively increased the fibre realignment until becoming an unidirectional scaffold.

As previously discussed, large values of applied strain induced drastic changes on the crystalline structure. In particular, the inner SAXS pattern evolved into a streak perpendicular to the fibre axis, indicating the development of macromolecular morphological alterations. This streak appeared at deformations of 200% for the random scaffold, see Fig. 9 (h), and

from deformations of 50% for the aligned scaffold stretched along MD, see Fig. 7 (f), (g) and (h). These values of deformation correlated with the drop of crystallinity, see Fig. 11. The streak provoked a substantial increment of the scattering signal, therefore at this stage the azimuthal integrations depicted in the polar plots had an additional component produced by the newly developed macromolecular arrangements, plotted by dash lines in Fig. 13, representative of the limitations of the current approach. The decoupling of the signal to obtain the fibre ODF for high applied strains requires careful assessment, as interpretation of the physical phenomena captured at this stage is not straightforward. As stated in the literature, the inner scattering signal may contain contributions from the microfibrillar structure, cavitations, voids and the surface scattering of the fibres [59, 30, 51, 52, 53, 54, 60]. Conventional void size for a broad range of materials including polyethylene and polyesters has been reported between 20 to 600 $\mathring{A}$, so cavitation could not be detected by SEM microscopy during this study. On the other hand, development of fibrils during fibre tensile stretching has been also reported as the main deformation micromechanism for aramids [30, 61] and aromatic copolysulfonamid [51], nevertheless, the observations obtained during our work could not solely attribute the evolution of the scattering to this mechanism, in agreement with recent publications in PCL fibre networks [34, 37]. In addition, in the particular case of scaffolds, the scattering in the vicinity of the beam center has been previously attributed to the difference in electron density between the nanofibres and air voids [31]. After cautious consideration, further research is needed at lower scales, including TEM observations [62], to determine the contribution of microvoids and fibrils development in the final plastic response of the material.

4. Conclusions

The deformation micromechanisms of electrospun polycaprolactone (PCL) tissue scaffolds were analyzed in detail by means of a combination experiments carried out at different length scales. Scaffolds with unidirectional (aligned) and random fibre Orientation Distribution Functions (ODFs) were manufactured by electrospinning and inspected by SEM microscopy. Spacial fibre distribution was ascertained by means of SAXS. Unidirectional

scaffolds presented an initial 90% of fibres oriented with the machine direction (MD), meanwhile the random scaffold had an isotropic fibre distribution. Fibre diameter was also higher for random scaffolds as a result of the lower processing velocity. Fibres were fused together by chemical bonds during manufacturing providing homogeneous connectivity to the fibre network. Scaffolds were subjected to tensile loads along perpendicular directions and although all configurations exhibited an initial elastic response followed by a yielding region, significant differences in mechanical properties were found as function of the initial fibre ODF. Aligned scaffolds stretched along the fibre direction (MD) presented the highest stiffness and strength compared to their perpendicular transverse direction (TD), meanwhile, the random scaffold possessed balanced mechanical properties for both principal directions.

Macromechanical deformation mechanisms at network level were identified as fibre straightening, rotation and stretching and they were responsible for the evolution of the fibre ODF. The aligned scaffold, with initial low fibre curvature, offered a different response depending on the loading direction, with predominance of fibre stretching or fibre rotation when elongated along MD or TD respectively. Plasticity at fibre level was directly proportional to fibre orientation with the loading direction, such that aligned fibres presented homogeneously distributed plasticity, and misaligned fibres exhibited localised necking. On the other hand, the random scaffold coupled fibre rotation and stretching with additional fibre straightening. The fibre curvature delayed the development of localised necking in misaligned fibres. Bond strength played a relevant role in the stress transfer between fibres, resulting in outstanding ductility of the scaffold, showing negligible bond fracture for strain levels of 200% as opposed to their counterparts thermally-bonded nonwoven fabrics.

Micromechanical deformation mechanisms at fibre level were determined as elastic and plastic fibre deformation, and final contribution into the mechanical response of the scaffold was ascertained by SAXS/WAXD diffraction techniques. PCL fibres presented an initial semicrystalline structure with an average of 56% crystal content. Upon deformation, elastic unfolding of amorphous chains was followed by plastic lamellae fragmentation and slippage, leading to macromechanical yielding of the scaffold. Fibre elasticity was registered by the evolution of the long period, meanwhile fibre plasticity was measured by the loss of crys-

tallinity. Macromechanical fibre straightening of initially curved fibres did not induce any change at fibre level, as determined by the evolution of the statistical long period of random scaffolds. After uncurling, scaffold elongation induced fibre elastic deformation until exhausting the mechanism. Above that threshold, fibre plasticity was triggered, finding a direct relationship between fibre alignment and loss of crystal content. Aligned scaffolds stretched along TD presented local fibre plasticity and necking with predominance of fibre rotation, inducing negligible loss of crystallinity. On the other hand, the aligned scaffold stretched along MD presented a progressive loss of crystal phase as a result of an homogeneous distribution of fibre plasticity. The random scaffold coupled both, elastic and plastic deformation, with predominance of fibre rotation and local necking up to a 100% of deformation, and predominance of fibre stretching for elongations higher than 100%, exhibiting an intrinsic loss of crystallinity. Finally, unidirectional scaffolds with highly oriented fibres subjected to large plastic deformation developed macromolecular fibrils and microvoids, as registered by the streak on two-dimensional SAXS patterns.

These detailed analyses of the micromechanisms of deformation in electrospun PCL scaffolds are critical to design engineering tissues with highly tunable and tailored mechanical properties for site specific *in vivo* applications . In particular, the influence of fibre curvature and spatial distribution as well as the bond density can be tailored to increase the individual contribution of fibres to the strength and toughness of the scaffold. Moreover, these analyses provide the basis for the study of the cyclic and fatigue response of the scaffold, where the contributions of elastic and plastic fibre deformations need to be ascertained.

5. Acknowledgements

This investigation was funded by the Diamond Light Source Synchrotron, [grant number 20494], the UK Regenerative Medicine Platform II, [grant number MR/L022974/1] and the MRC Computational and Chemical Biology of the stem cell Niche grant (CCBN) MR/L012766/1. FJCM acknowledges the support of the Erasmus Programme. JM acknowledges the Engineering and Physical Sciences Research Council (EPSRC) doctoral training partnership studentship, [grant number EP/N509644/1].

6. References

[1] Anica Lancuški, Frédéric Bossard, and Sébastien Fort. Carbohydrate-decorated PCL fibers for specific protein adhesion. *Biomacromolecules*, 14(6):1877–1884, 2013.

[2] J F Mano, G A Silva, H S Azevedo, and P B Malafaya. Natural origin biodegradable systems in tissue engineering and regenerative medicine: present status and some moving trends. *The Royal Society Interface*, 4(April):999–1030, 2007.

[3] Jorge M Sobral, Sofia G Caridade, Rui A Sousa, João F Mano, and Rui L Reis. Three-dimensional plotted scaffolds with controlled pore size gradients: effect of scaffold geometry on mechanical performance and cell seeding efficiency. *Acta biomaterialia*, 7(3):1009–1018, 2011.

[4] Sangamesh G Kumbar, Syam P Nukavarapu, Roshan James, Lakshmi S Nair, and Cato T Laurencin. Electrospun poly (lactic acid-co-glycolic acid) scaffolds for skin tissue engineering. *Biomaterials*, 29(30):4100–4107, 2008.

[5] Keith A Blackwood, Rob McKean, Irene Canton, Christine O Freeman, Kirsty L Franklin, Daryl Cole, Ian Brook, Paula Farthing, Stephen Rimmer, John W Haycock, et al. Development of biodegradable electrospun scaffolds for dermal replacement. *Biomaterials*, 29(21):3091–3104, 2008.

[6] Ilaria Palamà, Valentina Arcadio, Stefania D'Amone, Mariano Biasiucci, Giuseppe Gigli, and Barbara Cortese. Therapeutic PCL scaffold for reparation of resected osteosarcoma defect. *Scientific Reports*, 7:12672, 2017.

[7] Ana F M Pinheiro, Simone S Silva, Claudio Migliaresi, Márcia T. Rodrigues, Antonella Motta, Manuela E Gomes, Rui L Reis, and João F. Mano. Novel Genipin-Cross-Linked Chitosan/Silk Fibroin Sponges for Cartilage Engineering Strategies. *Biomacromolecules*, 9(10):2764–2774, 2008.

[8] Seung Hyun Ahn, Hyeong Jin Lee, and Geun Hyung Kim. Polycaprolactone scaffolds fabricated with an advanced electrohydrodynamic direct-printing method for bone tissue regeneration. *Biomacromolecules*, 12(12):4256–4263, 2011.

[9] M Janmohammadi and M Nourbakhsh. Electrospun polycaprolactone scaffolds for tissue engineering: a review. *International Journal of Polymeric Materials and Polymeric Biomaterials*, 68(9):1–13, 2018.

[10] Yong Bok Kim and Geun Hyung Kim. PCL/alginate composite scaffolds for hard tissue engineering: Fabrication, characterization, and cellular activities. *ACS Combinatorial Science*, 17(2):87–99, 2015.

[11] Robin Augustine, Susheel Kumer, Nandakumar Kalarikkal, Sabu Thomas, and Chittaranjan Patra. Electrospun polycaprolactone (PCL) scaffolds embedded with europium hidroxide nanorods (EHNs) with enhanced vascularization and cell proliferation for tissue engineering applications. *Journal of Materials Chemistry B*, 5(24), 2017.

[12] Sung Ju Cho, Sang Myung Jung, Munhyung Kang, Hwa Sung Shin, and Ji Ho Youk. Preparation of hydrophilic PCL nanofiber scaffolds via electrospinning of PCL/PVP-b-PCL block copolymers for

enhanced cell biocompatibility. *Polymer*, 69:95–102, 2015.

[13] Ko Eun Park, Beom Su Kim, Min Hee Kim, Hyung Keun You, Jun Lee, and Won Ho Park. Basic fibroblast growth factor-encapsulated PCL nano/microfibrous composite scaffolds for bone regeneration. *Polymer*, 76:8–16, 2015.

[14] LA Hidalgo-Bastida, JJA Barry, NM Everitt, FRAJ Rose, LD Buttery, IP Hall, WC Claycomb, and KM Shakesheff. Cell adhesion and mechanical properties of a flexible scaffold for cardiac tissue engineering. *Acta biomaterialia*, 3(4):457–462, 2007.

[15] João F M Ribeiro, Sara M Oliveira, José L Alves, Adriano J Pedro, Rui L Reis, Emanual M Fernandes, and Joao F. Mano. Structural monitoring and modeling of the mechanical deformation of three-dimensional printed poly (ϵ-caprolactone) scaffolds. *Biofabrication*, 9(025015), 2017.

[16] J. Lannutti, D. Reneker, T. Ma, D. Tomasko, and D. Farson. Electrospinning for tissue engineering scaffolds. *Materials Science and Engineering: C*, 27(3):504–509, 2007.

[17] Muhammad Anwaar Nazeer, Emel Yilgor, and Iskender Yilgor. Electrospun polycaprolactone/silk fibroin nanofibrous bioactive scaffolds for tissue engineering applications. *Polymer*, 168:86–94, 2019.

[18] Kadriye Tuzlakoglu, Catarina M Alves, Joao F Mano, and Rui L Reis. Production and Characterization of Chitosan Fibers and 3-D Fiber Mesh Scaffolds for Tissue Engineering Applications. *Macromolecular Bioscience*, 4:811–819, 2004.

[19] Megan O Chrobak, Katrina J Hansen, Joshua R Gershlak, Maria Vratsanos, Marianne Kanellias, Glenn R Gaudette, and George D Pins. Design of a fibrin microthread-based composite layer for use in a cardiac patch. *ACS Biomaterials Science Engineering*, 3(7):1394–1403, 2017.

[20] D. E. Discher, P. Janmey, and Y Wang. Tissue cells feel and respond to the stiffness of their substrate. *Science*, 310:1139–1143, 2005.

[21] F. Croisier, A. Duwez, C. Jérôme, A. Léonard, K. van der Werf, P. Dijkstra, and M. Bennink. Mechanical testing of electrospun PCL fibers. *Acta Biomateralia*, 8(1):218–224, 2012.

[22] Chantal Ayres, Gary L Bowlin, Scott C Henderson, Leander Taylor, Jackie Shultz, John Alexander, Todd A Telemeco, and David G Simpson. Modulation of anisotropy in electrospun tissue-engineering scaffolds: Analysis of fiber alignment by the fast Fourier transform. *Biomaterials*, 27(32):5524–5534, 2006.

[23] Geun Hyung Kim. Electrospun PCL nanofibers with anisotropic mechanical properties as a biomedical scaffold. *Biomedical Materials*, 3(2), 2008.

[24] Omaer Syed, Joong-Hyun Kim, Zalike Keskin-Erdogan, Richard M Day, Ahmed El-Fiqi, Hae-Won Kim, and Jonathan C Knowles. SIS/aligned fibre scaffold designed to meet layered oesophageal tissue complexity and properties. *Acta biomaterialia*, 99:181–195, 2019.

[25] Yunlei Yin and Jie Xiong. Effect of the Distribution of Fiber Orientation on the Mechanical Properties

of Silk Fibroin/Polycaprolactone Nanofiber Mats. *Journal of Engineered Fibers and Fabrics*, 12(3), 2017.

[26] Shing-Chung Wong, Avinash Baji, and Siwei Leng. Effect of fiber diameter on tensile properties of electrospun poly(ε-caprolactone). *Polymer*, 49(21):4713–4722, 2008.

[27] C. T. Koh, D. G T Strange, K. Tonsomboon, and M. L. Oyen. Failure mechanisms in fibrous scaffolds. *Acta Biomaterialia*, 9(7):7326–7334, 2013.

[28] Alvaro Ridruejo, Carlos González, and Javier Llorca. Micromechanisms of deformation and fracture of polypropylene nonwoven fabrics. *International Journal of Solids and Structures*, 48(1):153–162, 2011.

[29] Tahseen Kamal, Tae Joo Shin, and Soo Young Park. Uniaxial tensile deformation of poly(ϵ-caprolactone) studied with SAXS and WAXS techniques using synchrotron radiation. *Macromolecules*, 45(21):8752–8759, 2012.

[30] Xiaoyun Li, Feng Tian, Ping Zhou, Chunming Yang, Xiuhong Li, Fenggang Bian, and Jie Wang. In situ synchrotron small- and wide-angle X-ray study on the structural evolution of Kevlar fiber under uniaxial stretching. *RSC Advances*, 6(85):81552–81558, 2016.

[31] Takahiro Yano, Yuji Higaki, Di Tao, Daiki Murakami, Motoyasu Kobayashi, Noboru Ohta, Jun-ichiro Koike, Misao Horigome, Hiroyasu Masunaga, Hiroki Ogawa, and Yuka Ikemoto. Orientation of poly (vinyl alcohol) nano fiber and crystallites in non-woven electrospun nano fi ber mats under uniaxial stretching. *Polymer*, 53(21):4702–4708, 2012.

[32] E Zussman, M Burman, AL Yarin, R Khalfin, and Y Cohen. Tensile deformation of electrospun nylon-6, 6 nanofibers. *Journal of Polymer Science Part B: Polymer Physics*, 44(10):1482–1489, 2006.

[33] Matthew D. Edwards, Geoffrey R. Mitchell, Saeed D. Mohan, and Robert H. Olley. Development of orientation during electrospinning of fibres of poly(e-caprolactone). *European Polymer Journal*, 46(6):1175–1183, 2010.

[34] Alex M. Jordan and La Shanda T.J. Korley. Toward a tunable fibrous scaffold: Structural development during uniaxial drawing of coextruded poly(ϵ-caprolactone) fibers. *Macromolecules*, 48(8):2614–2627, 2015.

[35] C. Lim, E. Tan, and S. Ng. Effects of crystalline morphology on the tensile properties of electrospun polymer nanofibers. *Applied Physics Letters*, 92(14):141908, 2008.

[36] W. Yee, A. Nguyan, P. Lee, M. Kotaki, Y. Lim, B. Tan, and et al. Stress-induced structural changes in electrospun polyvinylidene difluoride nanofibers collected using a modified rotating disk. *Polymer*, 49(19):4196–4203, 2008.

[37] Hua Mo Yin, Yan Fei Huang, Yue Ren, Peng Wang, Baisong Zhao, Ji Hua Li, Jia Zhuang Xu, and Zhong Ming Li. Toward biomimetic porous poly(ϵ-caprolactone) scaffolds: Structural evolution and morphological control during solid phase extrusion. *Composites Science and Technology*, 156:192–202,

2018.

[38] James A Reid and Anthony Callanan. Hybrid cardiovascular sourced extracellular matrix scaffolds as possible platforms for vascular tissue engineering. *Journal of Biomedical Materials Research Part B: Applied Biomaterials*, 2019.

[39] H Hatakeyama, T Yoshida, and T Hatakeyama. The effect of side chain association on thermal and viscoelastic properties: cellulose acetate based polycaprolactones. *Journal of Thermal Analysis and Calorimetry*, 59(1-2):157–168, 2000.

[40] Ángel Alvaredo, María Isabel Martín, Pere Castell, Roberto Guzmán de Villoria, and Juan P Fernández-Blázquez. Non-Isothermal Crystallization Behavior of PEEK/Graphene Nanoplatelets Composites from Melt and Glass States. *Polymers*, 11(1):124, 2019.

[41] Diamond Light Source. B22 beamline description, 2019.

[42] Mark Basham, Jacob Filik, Michael T Wharmby, Peter CY Chang, Baha El Kassaby, Matthew Gerring, Jun Aishima, Karl Levik, Bill CA Pulford, Irakli Sikharulidze, et al. Data analysis workbench (DAWN). *Journal of Synchrotron Radiation*, 22(3):853–858, 2015.

[43] J Filik, AW Ashton, PCY Chang, PA Chater, SJ Day, M Drakopoulos, MW Gerring, ML Hart, OV Magdysyuk, S Michalik, et al. Processing two-dimensional X-ray diffraction and small-angle scattering data in DAWN 2. *Journal of Applied Crystallography*, 50(3):959–966, 2017.

[44] 2016.

[45] K. Sownthari and S. A. Suthanthiraraj. Synthesis and characterization of an electrolyte system based on a biodegradable polymer. *Express Polymer Letters*, 7(6):495–504, 2013.

[46] F Cser. About the Lorentz correction used in the interpretation of small angle X-ray scattering data of semicrystalline polymers. *Journal of Applied Polymer Science*, 80(12):2300–2308, 2001.

[47] Naigeng Chen, Margaret KA Koker, Simge Uzun, and Meredith N Silberstein. In-situ X-ray study of the deformation mechanisms of non-woven polypropylene. *International Journal of Solids and Structures*, 97:200–208, 2016.

[48] Juan C Fernández-Toribio, Belén Alemán, Álvaro Ridruejo, and Juan J Vilatela. Tensile properties of carbon nanotube fibres described by the fibrillar crystallite model. *Carbon*, 133:44–52, 2018.

[49] Francisca Martínez-Hergueta, Álvaro Ridruejo, Carlos González, and Javier Llorca. Deformation and energy dissipation mechanisms of needle-punched nonwoven fabrics: A multiscale experimental analysis. *International Journal of Solids and Structures*, 64–65:120–131, 2015.

[50] Rana Rezakhaniha, Aristotelis Agianniotis, Jelle Tymen Christiaan Schrauwen, Alessandra Griffa, Daniel Sage, CVC vd Bouten, FN Van De Vosse, Michaël Unser, and Nikolaos Stergiopulos. Experimental investigation of collagen waviness and orientation in the arterial adventitia using confocal laser scanning microscopy. *Biomechanics and Modeling in Mechanobiology*, 11(3-4):461–473, 2012.

[51] Xiaoyun Li, Jinchao Yu, Jianning Wang, Kang Chen, Xiuhong Li, Yumei Zhang, Fenggang Bian, and Jie Wang. Structure and performances changes during tensile of aromatic copolysulfonamide fibers under different thermal temperatures via in-situ synchrotron SAXS/WAXS. *European Polymer Journal*, 98(November 2017):354–361, 2018.

[52] N. S. Murthy, C. Bednarczyk, R. A.F. Moore, and D. T. Grubb. Analysis of small-angle X-ray scattering from fibers: Structural changes in nylon 6 upon drawing and annealing. *Journal of Polymer Science, Part B: Polymer Physics*, 34(5):821–835, 1996.

[53] Andrzej Pawlak and Andrzej Galeski. Plastic deformation of crystalline polymers: The role of cavitation and crystal plasticity. *Macromolecules*, 38(23):9688–9697, 2005.

[54] A. Reyes-Mayer, B. Alvarado-Tenorio, A. Romo-Uribe, R. Benavente, M. Jaffe, and A. Molina-Ocampo. Nanostructure reorganization in a thermotropic copolyester. A simultaneous WAXS and SAXS study. *Polymers for Advanced Technologies*, 27(6):748–758, 2016.

[55] Sajjad Shafei, Javad Foroughi, Leo Stevens, Cynthia S Wong, Omid Zabihi, and Minoo Naebe. Electroactive nanostructured scaffold produced by controlled deposition of PPy on electrospun PCL fibres. *Research on Chemical Intermediates*, 43(2):1235–1251, 2017.

[56] Alvaro Ridruejo, Carlos González, and Javier Llorca. Failure locus of polypropylene nonwoven fabrics under in-plane biaxial deformation. *Comptes Rendus Mecanique*, 340(4-5):307–319, 2012.

[57] Yongfeng Men and Jens Rieger. Role of the entangled amorphous network in tensile deformation of semicrystalline polymers. *Physical Review Letters*, 91(9), 2003.

[58] AJ Smith, LS Davidson, JH Emmins, JC Bardsley, P Holloway, M Malfois, AR Marshall, CL Pizzey, SE Rogers, O Shebanova, et al. I22: SAXS/WAXS beamline at Diamond Light Source–an overview of 10 years operation. *arXiv preprint arXiv:1903.05405*, 2019.

[59] Guillermo Jimenez, Nobuo Ogata, Hidekazu Kawai, and Takashi Ogihara. Structure and thermal/mechanical properties of poly(ϵ-caprolactone)-clay blend. *Journal of Applied Polymer Science*, 64(11):2211–2220, 1997.

[60] Angel Romo-Uribe, Adriana Reyes-Mayer, Manuela Calixto-Rodriguez, Rosario Benavente, and Michael Jaffe. Synchrotron scattering and thermo-mechanical properties of high performance thermotropic polymer. A multi-scale analysis and structure-property correlation. *Polymer*, 153:408–421, 2018.

[61] S Ran, D Fang, X Zong, B. S. Hsiao, B Chu, and Philip M Cunniff. Structural changes during deformation of kevlar via online syncrotron SAX/WAXD techniques. *Polymer*, 42:1601–1612, 2001.

[62] A. Galeski, A. S. Argon, and R. E. Cohen. Changes in the morphology of bulk Spherulitic nylon 6 Due to plastic deformation. *Macromolecules*, 21(9):2761–2770, 1988.